

**iScience, Volume 23**

## **Supplemental Information**

### **Seeing Natural Images through the Eye of a Fly with Remote Focusing Two-Photon Microscopy**

**Anna Schuetzenberger and Alexander Borst**

## Supplemental Information

### Supplemental Figures

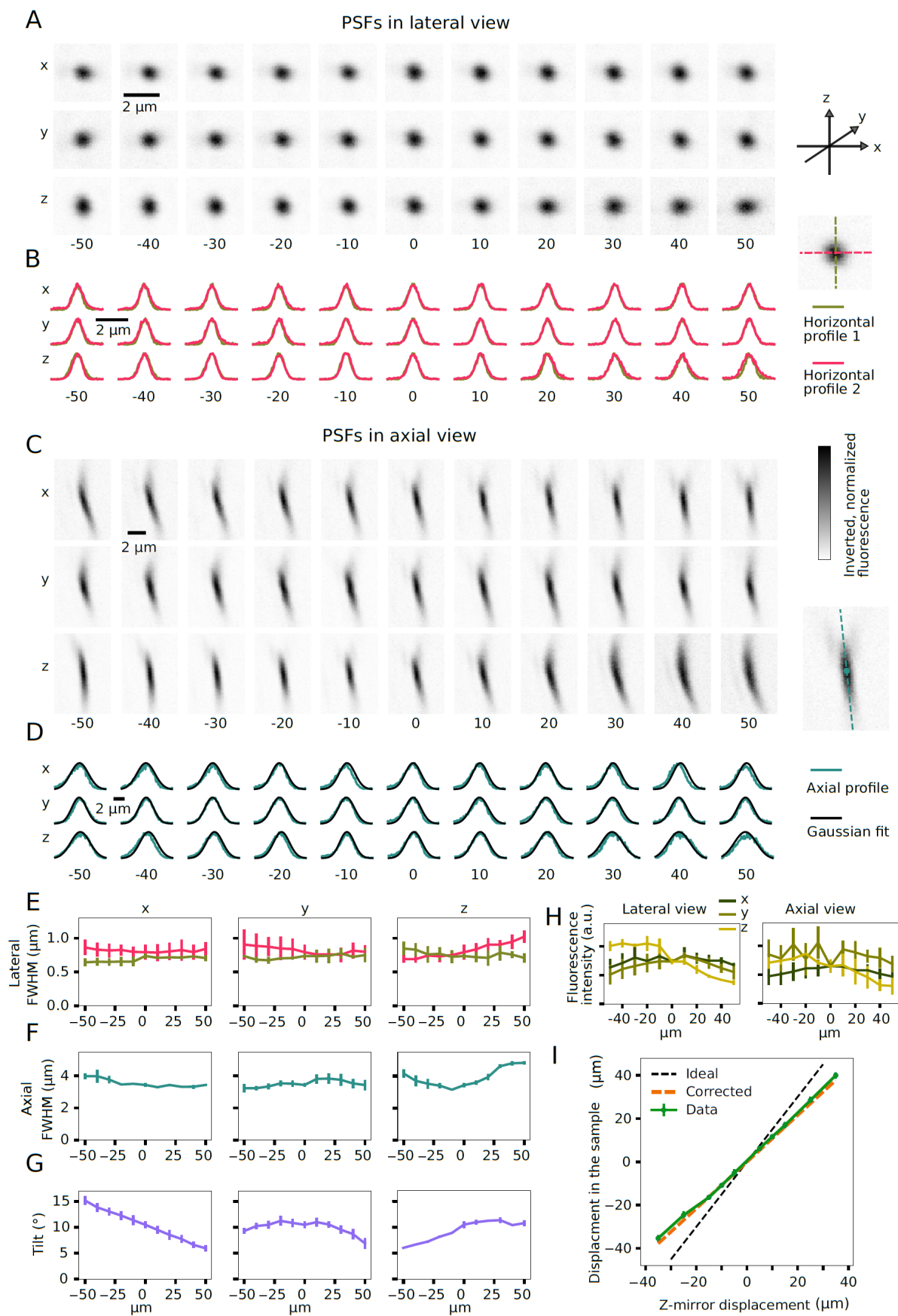


**Figure S1 | Point spread function measurements. Related to Figure 2.** a) Lateral (xy) view of 0.1  $\mu\text{m}$  fluorescent beads at ten positions along each axis (x, y and z). Mean images of three measurements. b) 1D profiles of the images in a) A 1D Gaussian function was fitted to each bead's profile to determine its full width at half maximum (FWHM). c) Axial (xz) view of 0.1  $\mu\text{m}$  fluorescent beads at ten positions along each axis (x, y and z). Mean images of three measurements. d) A 2D Gaussian was fitted to each bead image. The mean profile along the elongated axis (turquoise) and the Gaussian fit along this axis (black) are shown. e) Lateral FWHM of the beads in a). Left, middle and right panel show the measurements along the x-, y- or z-axis, respectively. f) Axial FWHM of the beads in c). Left, middle and right panel show the measurements along the x-, y- or z-axis, respectively. g) Angle relative to 90° of the 2D Gaussian fit of the beads in c). Left, middle and right panel show the measurements along the x-, y- or z-axis, respectively. h) Relative fluorescence intensity of the beads. Left: Intensity of the bead center along different axes as in a). Right: Intensity of the bead center along the different axes as in c). i) Displacement of a bead in the imaging volume upon z-mirror displacement. The empirical measurements (green) were fitted with a linear model (orange). The slope of the linear fit rather than the ideal slope was used as a parameter in our imaging software to ensure accurate lengths and plane transformations.

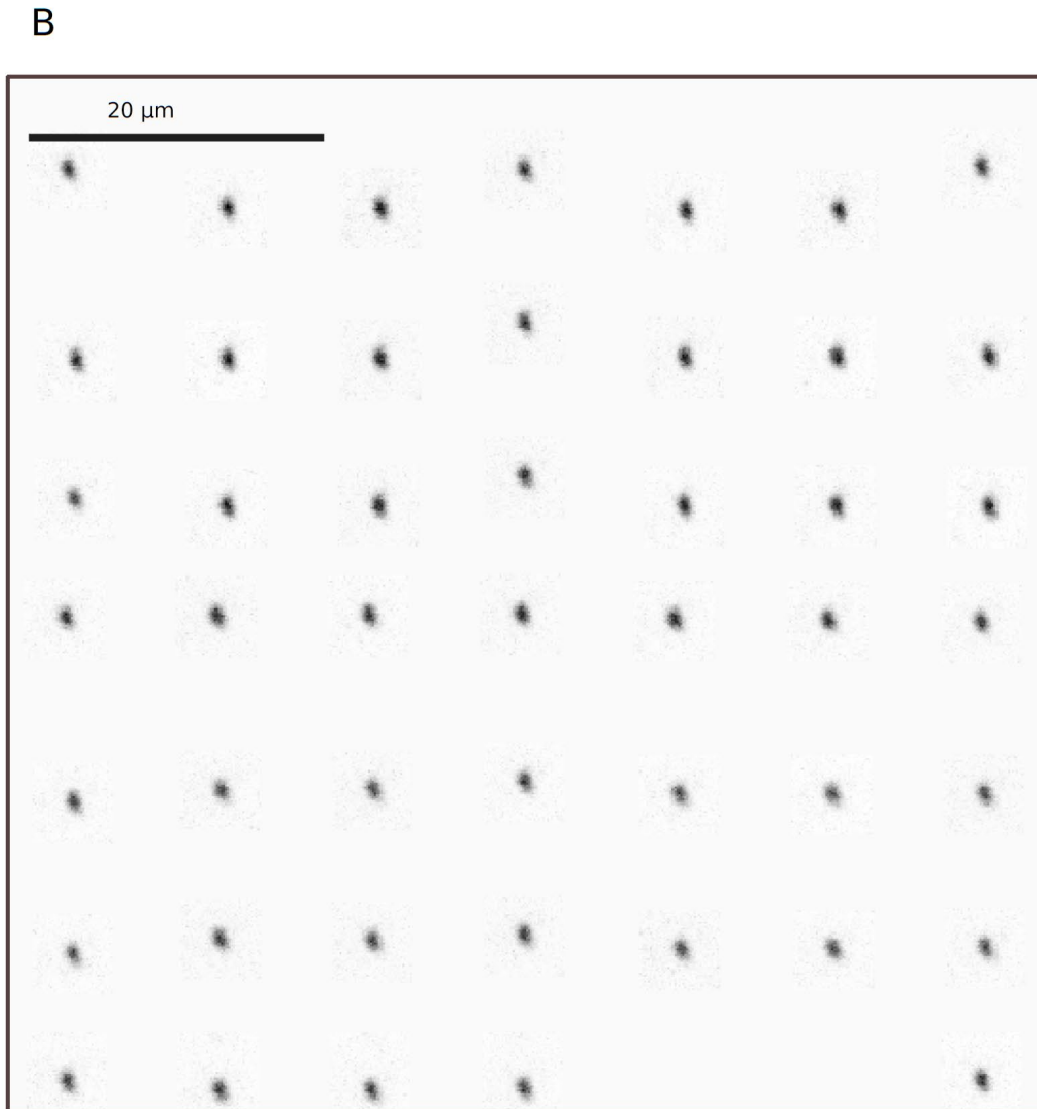
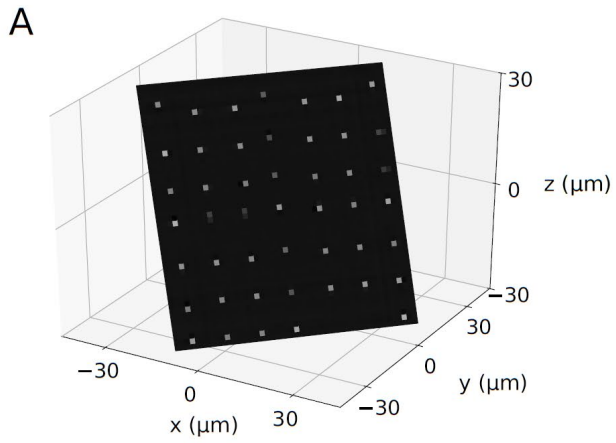


**Figure S2 | Point spread functions in an oblique cross-section. Related to Figure 2.** Composite image of 0.1  $\mu\text{m}$  fluorescent beads imaged in different positions in an oblique imaging plane. This plane is tilted by  $45^\circ$  around the  $z$ -axis, followed by  $55^\circ$  around the  $x$ -axis, as illustrated in the top panel. It corresponds to a typical rotation and zoom we used to image planes in the fly visual system.

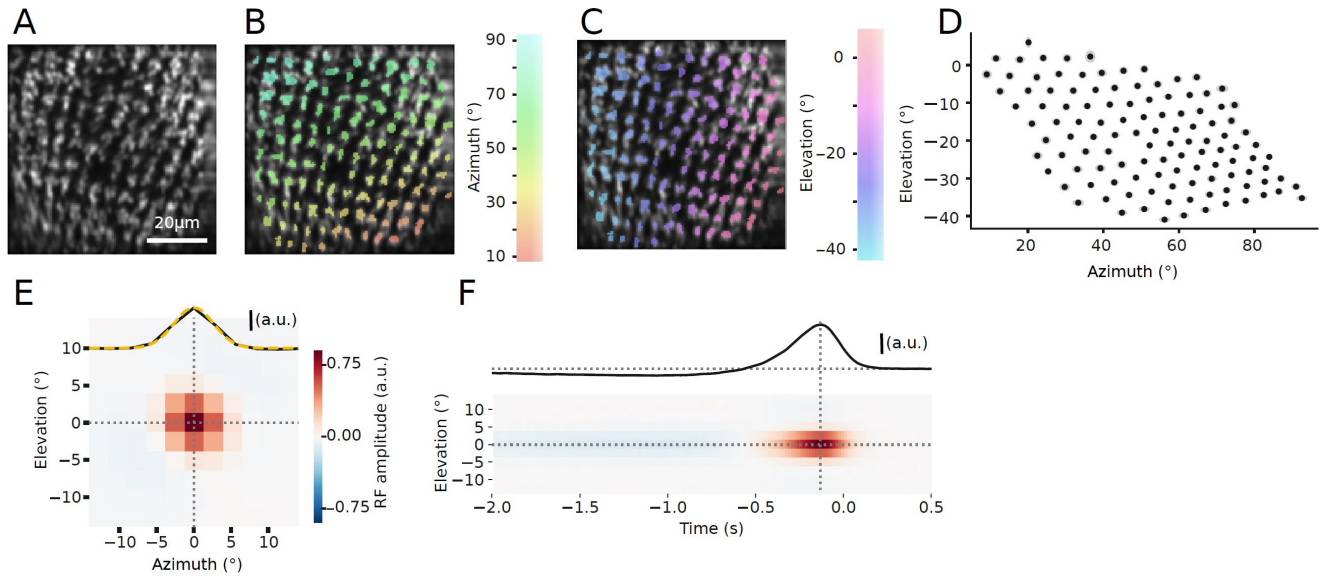


**Figure S3 | Receptive field of Mi1. Related to Figure 3.** a) Mean image of a recording of Mi1 axon terminals in layer 10 of the medulla expressing GCaMP6f. b) Axon terminals colored by their receptive field location in azimuth. c) Axon terminals colored by their receptive field location in elevation. d) Receptive field locations (black dots) with receptive field size (sigma of Gaussian fit, grey shaded areas) of all cells in the example recording also shown in a)-c). e) Average spatial receptive field of all cells ( $N = 8$  flies,  $n = 540$  cells). The profile in azimuth (black line) was fitted with a Gaussian (yellow). Average receptive field size was  $2.02 \pm 0.3^\circ$  ( $\sigma$  of the Gaussian fit, corresponding to  $4.77 \pm 0.7^\circ$  FWHM). f) Temporal profile of the receptive field. Grey dashed lines indicate the maximum receptive field amplitude.

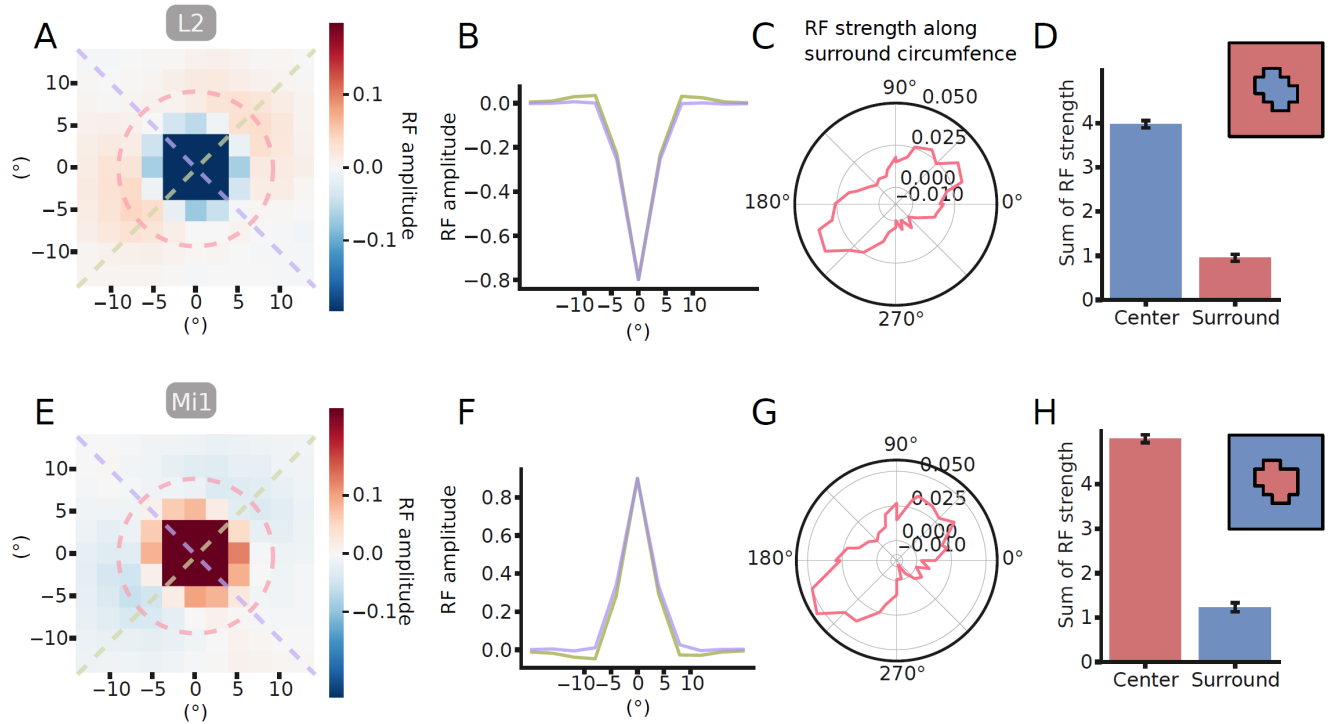


**Figure S4 | Anisotropic spatial receptive fields. Related to Figure 3.** a) Mean L2 receptive field (RF) with cropped color map, showing the anisotropic surround. The profiles along the colored dashed lines are plotted in b and c. b) 1D profile through the diagonal axes of the RF, as indicated in a. c) RF strength along the circumference of the RF indicated in a. A clear anisotropy can be observed. d) Relative RF strength of the center and the surround. All values of the RF center (blue area in inset) summed up result in the center RF strength. All values of the RF surround (red area in inset) summed up result in the surround RF strength. The surround accounts for 1/5<sup>th</sup> of the RF strength. e-f) Analogous for Mi1 as a-d) for L2. For better comparison, the data in the polar plot in g) was multiplied by -1.

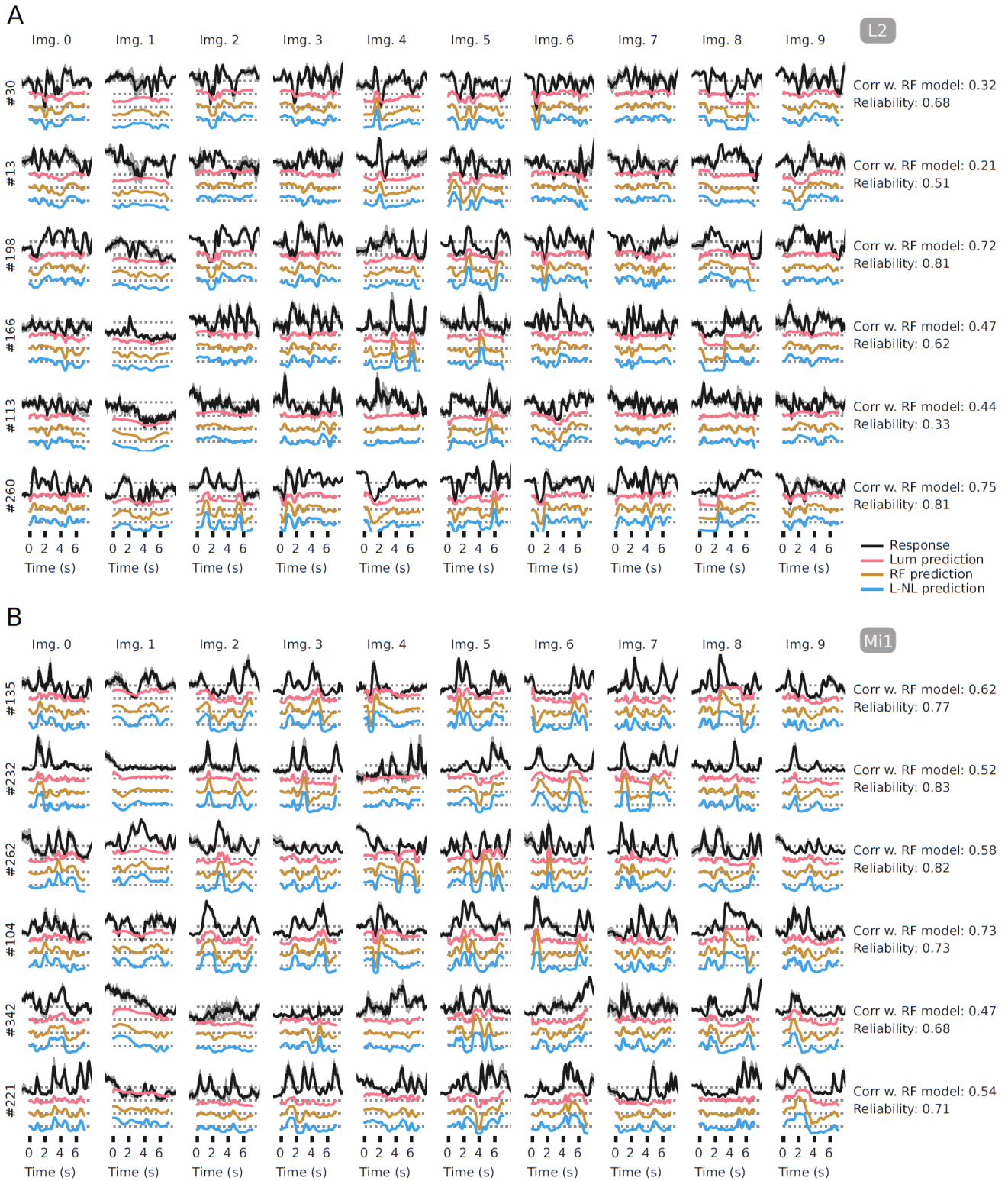


**Figure S5 | Moving image example responses. Related to Figure 5.** a) More example responses of L2 to moving images together with the corresponding model responses as in Fig. 5b. The y-axis label indicates the cell number. The dashed grey lines indicate the relative zero lines for the respective models. b) Analog to a) for Mi1.



## Supplemental tables

Static images	Mean	STD	95 % confi. Interv.	Student's t-test p-value
Reliability peak	0.89	0.05	0.01	8.14E-34
Lum model peak	0.79	0.11	0.01	
Reliability sust.	0.59	0.22	0.02	0.005220031
Lum model sust.	0.63	0.19	0.02	

**Table S1 | Statistics related to Figure 4.**

**L2**

Model correlations	Mean*	STD	95 % confi. Interv.
Reliability	0.54	0.26	0.03
Lum model	0.36	0.15	0.02
RF model	0.45	0.15	0.01
L-NL model	0.45	0.15	0.01
Student's t-test p-value			
Lum vs RF model	1.49E-17		
RF vs. L-LN model	0.95646		

**Mi1**

Model correlations	Mean*	STD	95 % confi. Interv.
Reliability	0.71	0.19	0.02
Lum model	0.54	0.11	0.01
RF model	0.57	0.10	0.01
L-NL model	0.57	0.10	0.01
Student's t-test p-value			
Lum vs RF model	0.003096		
RF vs. L-LN model	0.303808		

\* Pearson's correlation coefficient r

Nonlinearity: logistic function fitted parameters			
$b_u$	$b_l$	$x_0$	k
174.33	-4.18	14.72	0.25

Nonlinearity: logistic function fitted parameters			
$b_u$	$b_l$	$x_0$	k
1.50	-0.84	0.30	2.54

**Table S2 | Detailed statistics and model parameters related to Figure 5.**

## Transparent Methods

### Experimental animals

*Drosophila melanogaster* were kept on standard cornmeal-agar medium at 25° and at 60 % relative humidity in a 12/12 h light/dark cycle. The Gal4-UAS system (Brand and Perrimon, 1993) was used to express GCaMP6f (Chen et al., 2013) in the lamina cell type L2 and the medulla cell type Mi1. The resulting genotype of the L2 experimental flies was  $w^+/w^-$ ; R53G02-AD/UAS-GCaMP6f; R29G11-DBD/UAS-GCaMP6f, and of the Mi1 experimental flies was  $w^+/w^-$ ; R19F01-AD/UAS-GCaMP6f; R71D01-DBD/UAS-GCaMP6f. Female flies 1-7 days after eclosion were used for the experiments.

### Remote-focusing two-photon microscopy

We designed a remote-focusing two-photon microscope based on the two-photon microscope described in Euler et al. (2009) and the principle of remote focusing described in Botcherby et al. (2008).

#### *Basic two-photon system*

A MaiTai eHP DS Ti:Sapphire oscillator was used as a laser source. A beam attenuator (Newport VA-BB-2-CONEX) was used to control the laser intensity, and a telescope initially collimated the beam and widened it approximately 4-fold. The lateral scan unit comprised of two galvanometer optical scanners (Cambridge Technologies 6215H). A telescope then magnified the beam with magnification  $M_1 = 4$  and imaged it to the back aperture of the sample objective lens. The water immersion Olympus Lumplfln 40x w with an NA of 0.8, back aperture of 9 mm and working distance of 3.3 mm was used as sample objective lens. A Photomultiplier Tube (Hamamatsu H10770-PB40) collected the emitted fluorescence signal, which was then digitized with a NI PCI-6110 data acquisition board. A band-pass filter (BrightLine 514/30) and a short-pass filter ensured that light from the visual stimulation arena and the laser could not reach the photomultiplier tube.

#### *Remote focusing module*

The remote focusing module was positioned in the beam path after the attenuator and the initial telescope, and before the lateral scan unit. The beam enters the module at a polarization-based beam splitter (PBS). It then passes through a  $\lambda/4$  plate, enters the remote objective lens, is reflected by the z-mirror, and travels back through the remote objective lens and the  $\lambda/4$  plate. It is in turn reflected by the PBS and passed through the telescope to the lateral scan unit.

The position of the z-mirror with respect to the focal plane of the remote objective lens was controlled by a piezoelectric actuator and a closed-loop DSP controller. The actuator was manufactured customized (nanoFaktur) to have a fast settling time (1 ms at 1  $\mu\text{m}$  precision) at a large traveling range (280  $\mu\text{m}$ ) and a position sensor. A DSP Controller (nPoint LC.402 with extended current) was used to control the actuator. The

z-mirror was glued on the actuator. We chose a lightweight mirror (Thorlabs PF05-03-M01, 12mm diameter) that can tolerate the laser intensities needed for calcium imaging. Since the laser beam diameter on the mirror is very small (down to  $<1 \mu\text{m}$  if the mirror position is exactly in the focal plane), the energy per area is large. In addition, for mode-locked laser sources with femtosecond pulse length, damage thresholds were not determined by the manufacturer. Therefore, we tested several different mirrors for applicability in this specific setting. Metal-coated mirrors were found to be superior to dielectric mirrors. The actuator together with the z-mirror were mounted on a XYZ translation stage (Thorlabs PT3/M). This enabled a simple manual translation of the z-mirror and actuator in the case of local mirror damage. We tuned the PDI controller of the piezo to optimize for scanning distances of around  $90 \mu\text{m}$ , which it could achieve with sufficient precision up to 15 Hz. Alternatively, we used it to scan smaller size planes ( $50 \times 50 \mu\text{m}$ ) at up to 20 Hz. Depending on the use, the PDI controller could also be tuned to optimize for shorter scanning distances, where it then could achieve still higher scan rates.

As the remote objective lens (ROL), we chose a Leica HC PLAN APO objective with 40x magnification, 0.85 NA, 0.21 mm free working distance and transmission of about 70% at 920 nm. Since the sample objective lens is a water immersion objective, we could not use the exact same model for the remote focusing lens. To account for the cover slip correction of this lens, we mounted a cover slip to its front.

Two telescopes imaged the back aperture of the remote objective lens onto the back aperture of the imaging objective lens, with an intermediate conjugate plane close to the lateral scan unit. The focal lengths of the relay lenses were  $f_1 = 125 \text{ mm}$ ,  $f_2 = 40 \text{ mm}$ ,  $f_3 = 50 \text{ mm}$  (scan lens),  $f_4 = 200 \text{ mm}$  (tube lens). Together with the focal lengths of the objective lenses, 5 mm for the ROL and 4.5 mm for the IOL, this resulted in an overall magnification of

$$\frac{f_{ROL}}{f_1} * \frac{f_2}{f_3} * \frac{f_4}{f_{IOL}} = \frac{5}{125} * \frac{40}{50} * \frac{200}{4.5} = 1.42$$

which is close to the desired value for aberration-free imaging of  $n_2/n_1 = 1.33$  (Botcherby et al., 2007).

The distances between the lenses in the relay system were: Back end of ROL to  $f_1$ : 125 mm;  $f_1$  to  $f_2$ : 165 mm;  $f_2$  to  $f_3$ : 90 mm;  $f_3$  to  $f_4$ : 250 mm;  $f_4$  to back end of IOL: 95 mm. The distance between  $f_4$  and IOL could vary by few mm, depending on the precise positioning of the sample. Apart from the last distance, all distances were chosen as to ensure a 4f telecentric configuration. This last distance is often set in conventional two-photon microscopes to be smaller than the sum of the focal distances of tube lens and objective lens. While entirely aberration-free imaging is only possible with 4f relays (Botcherby et al., 2008), the optical resolution and linearity in our system across the relevant imaging range were only marginally affected, which is why we decided to keep this configuration.

### *Validation*

To validate the resolution and scaling along the z-axis, we imaged 1  $\mu\text{m}$  and 0.1  $\mu\text{m}$  diameter fluorescent beads (Polysciences Fluoresbrite) embedded in agarose. The approximate theoretical resolution limit of an imaging system, i.e. the minimum distance between two points to be resolvable, is given by the Rayleigh criterion (adapted for two-photon microscopy, see Yang and Yuste, 2017):

$$R_{xy} = \frac{0.4 \lambda}{NA} = 0.46 \mu\text{m}$$

$$R_z = \frac{1.4 \lambda n}{NA^2} = 2.7 \mu\text{m}$$

Where NA is the numerical aperture of the objective lens,  $\lambda$  is the wavelength and n the refractive index of the imaging medium. The cross-sections of a bead were measured at different points in a 100x100x100  $\mu\text{m}$  volume. A 2D Gaussian was fitted to each cross-section, and the full width at half maximum (FWHM) was defined as the resolution of the system.

To measure the scaling factor between mirror movement and focal spot displacement in z, we focused on an individual bead, moved the z-mirror by a set amount, and then measured the distance we needed to move the IOL with a micromanipulator to bring the bead back in focus (Fig. S2i). The resulting scaling factor was used by the software to ensure appropriate distances and transformations. The scaling factor for a perfect imaging system from air to water is 1.5 (Botcherby et al., 2012, 2008). The empirically determined factor for our system was 1.1. The transformation was near linear across 90  $\mu\text{m}$  of focal spot displacement (Fig. S2i).

### *Software*

A customized version of the open-source software ScanImage 5.1 (Pologruto et al., 2003) was used to acquire the data. NI data acquisition boards were used to generate the output voltage for the mirrors (PCIe-6353 with two BNC 2110 accessories) and to collect the signal from the photomultiplier tube. In a second input channel, the trigger signal for synchronization of the visual stimulus with the imaging data was recorded. We extended the functionality of ScanImage (Matlab2013b) to control the movement of the piezo actuator for scanning in z in the same way as it controls the galvanometer motors for lateral scanning. A third output channel generated the voltage that defined the position of the z-mirror. A scaling parameter (0.0565 V/ $\mu\text{m}_z$ , determined empirically, see above) ensured the appropriate transformation of voltage to the axial displacement in the sample space. ScanImage represents an imaging plane as a time series of 2D vectors, the positions of the focal point in a virtual space. The first and second dimension correspond to the movement of the x and y scan mirrors, respectively. We added a third dimension to this representation. Simple rotation matrix transformations applied to the 3D vectors can then arbitrarily rotate the imaging plane in 3D space, about

several rotational axis simultaneously. In addition, since the piezo motor moving the z mirror is slower than the galvanometer motors, we ensured that the z-mirror receives only the slow part of scanning signal. With additional rotational controls in the graphical user interface, the user can rotate the imaging plane in the 3D imaging volume in all directions during imaging. Our modified version of ScanImage is publicly available on Github under [https://github.com/borstlab/Scanimage\\_Planes3D](https://github.com/borstlab/Scanimage_Planes3D).

#### Visual stimulation arena

For the display of visual stimuli to the fly, we used a custom-build projector-based arena as described previously (Arenz et al., 2017). Briefly, visual stimuli were projected onto a semi-transparent cylinder that was positioned in front of the fly, spanning 180° in azimuth and 105° in elevation of the fly visual field. Stimuli were projected with a frame rate of 180 Hz in 255 brightness steps. The brightest absolute luminance of the arena reached approximately 250 candela/m<sup>2</sup>, and the wavelength was restricted to > 550 nm, to separate it from the GCaMP emission wavelength. Stimuli were written in Python 2.7 using the Panda3D software. To synchronize the visual stimulation with data acquisition, a small corner of the arena displayed a trigger signal that was recorded together with the imaging data.

#### Visual stimuli and natural images datasets

##### *Letter stimulus*

The letter stimulus consisted of 30x30° large, bright letters on a dark background. The letters were flashed following a completely dark background, for 1 second. Each letter was presented three times.

##### *White noise stimulus*

To determine the linear receptive field of the neurons, a white noise stimulus was shown for 4-10 minutes. The stimulus consisted of a grid of 64x54 pixels, each pixel corresponding to approximately 2.8x1.9° in visual space. The luminance of each pixel changed every third frame according to values (0-255) drawn from a normal distribution. The luminance values were then slightly low-pass filtered in space and time ( $\tau = 0.5$  s). For a subset of acquisitions, the luminance of each pixel could either take the value 0 or 255, set by a pseudo-random number generator every 0.5 s ("binary noise stimulus").

##### *Static natural scenes stimulus*

We used images from the Van Hateren natural image dataset (van Hateren and van der Schaaf, 1998) for the static natural scenes stimulus. Of the 4000 images in the dataset, we selected 50 images that represented the image diversity and showed variable luminance and contrast characteristics. The images were then cropped, downsampled to 180x260 px (corresponding to approx. 1x0.4° in the fly's visual space) and gamma corrected ( $\gamma=1.5$ ) to compress the luminance range to the 8 bit depth of the stimulation arena.

At the beginning of each trial, following a gray screen (luminance = 125), an image was displayed on the full screen. The image stayed for 1.5 seconds before the screen turned gray again. To compare the image responses to luminance steps, we added two additional stimulus conditions. Following a gray background, either a black screen (luminance = 0, OFF flicker stimulus) or a white screen (luminance = 255, ON flicker stimulus) was shown for 1.5 seconds. This resulted in a total of 52 stimulus conditions in the natural scenes stimulus. Each stimulus condition was repeated three times and trials were randomized for each acquisition.

#### *Moving natural scenes stimulus*

Ten 360° panoramic images from an HDR image dataset (Brinkworth and O'Carroll, 2009) were used for the moving natural scene stimulus. The images were gamma corrected ( $\gamma=2.2$ ) to compress the luminance range to the 8 bit depth of the stimulation arena and slightly stretched along the elevation axis to cover the entire 105° vertical extend of the stimulus arena (original images spanned 75° in vertical extend). The images were displayed on the arena and, after two seconds, started moving first to the left for seven seconds, and then back (to the right) for another seven seconds (For one recording of Mi1, the image moved for only six seconds, stopped for two seconds and then moved back for six seconds. Only the first six seconds of all recordings were analyzed). Each image was shown in three trials, and all trials were randomized. For a new acquisition, the image phase in azimuth at which the image started to move was randomized to increase stimulus variability and avoid artificially introduced correlations between acquisitions. An example stimulus together with cellular responses is shown in the supplemental video.

#### Calcium imaging procedure

Flies were prepared for imaging following a standard procedure (Maisak et al., 2013). Briefly, flies were anesthetized on ice and then glued to a holder with the posterior side of the head exposed to the objective lens through a small opening. Ringer's solution was applied, and the cuticle, fat and trachea at the back of the head were removed for optical access.

Initially, a moving grating was shown to locate areas of axon terminals with large calcium responses. The imaging plane was then rotated with the rotational controls in the ScanImage GUI until the plane spanned by the 2D array of axon terminals was visible. Then, the white noise stimulus was shown, followed by either the static or the moving natural scenes stimulus. For a subset of acquisitions, we showed a white noise stimulus again after the natural images stimulus, to verify that the receptive field locations of the cells had not changed. Recordings were terminated prematurely if cells stopped showing calcium responses, and data from these recordings were not used for further analysis. All data were recorded at a frame rate of 7.5 Hz and a zoom setting of 3 (for L2) or 4 (for Mi1), equivalent to a field of view size of about 90 or 70  $\mu\text{m}$ , respectively.

For the letter stimulus, we first used a small, windowed grating stimulus to approximately locate the area on the screen the cell population responded to. We then placed the letter stimulus at that location. Fig. 2f shows average  $\Delta F/F$  images over one second duration of the letter and over three trials.

#### Data processing and analysis

Data analysis was performed in Python 2.7 with custom-written software.

##### *Preprocessing*

Image sequences were registered to the mean image with a phase correlation algorithm described in detail in Arenz et al., (2017). For L2, individual cells' axon terminals were selected based on initial thresholding of the high-pass filtered mean image, followed by manual inspection and corrections. For Mi1, individual cells' axon terminals were selected using a custom-written algorithm based on correlations between neighboring pixels in the white noise experiment and thresholding, followed by manual inspection and correction.

##### *White noise analysis*

For baseline subtraction, a dynamic baseline fluorescence level was determined by low-pass filtering ( $\tau = 5$  s) the raw fluorescence signal for each cell. The baseline was then shifted by in time by  $\tau * \text{framerate}/2$  and subtracted from the raw fluorescence signal, resulting in the calcium signal  $\Delta F$ . For each cell, reverse correlation of the calcium signal to the white noise stimulus was then performed, described in detail in Arenz et al. (2017), resulting in the spatio-temporal linear receptive field (RF). A 1D Gaussian function was fitted to the azimuth and the elevation axes of the spatial RF. The peaks of the curve fits were termed the RF location of each cell. RFs were normalized and cells with a z-score  $< 10$  and recordings with the binary noise stimulus were not included in the white noise analysis (Fig. 3, Fig. S3 and S4). For the natural scenes analyses, cells with RFs with a z-score  $< 7$  were not included (Fig. 4 and Fig. 5).

##### *Static natural scenes analysis*

For each cell, the raw fluorescence signal in the second before the start of a trial was used as baseline and subtracted from the fluorescence signal during that trial. Subsequently, responses to three trials were averaged to obtain the mean response for each stimulus condition. Cells that exhibited very small responses to ON and OFF flicker stimuli ( $< 200$  difference in baseline-subtracted raw fluorescence units), and cells with a standard deviation of trial-to-trial correlation coefficients of  $> 0.04$  were excluded from further analysis. The peak and sustained responses,  $R_{\text{peak}}$  and  $R_{\text{sust}}$ , were quantified as follows:

$$R_{\text{peak}} = \begin{cases} \min(\Delta F_s) & \text{if } |\min(\Delta F_s)| > |\max(\Delta F_s)| \\ \max(\Delta F_s) & \text{if } |\min(\Delta F_s)| < |\max(\Delta F_s)| \end{cases}$$

$$R_{sust} = \text{mean}(\Delta F_{s,t>1})$$

With  $\Delta F_s$  being the calcium signal during the stimulus presentation, and  $\Delta F_{s,t>1}$  the calcium signal during the last 0.5 s of stimulus presentation. The calcium signals and the response quantifications were then divided by a normalization factor. The factor was defined for each cell as 4 times the standard deviation of  $R_{sust}$  over all stimulus conditions.

For each cell, we fitted a linear function to its mean image responses (50 data points) and the image luminance at its RF using the least squares method. How well the fit could predict the data was expressed as the mean of the Pearson's correlation coefficient  $\rho$  between fit and each of the three trials:

$$\rho_{fit} = \frac{\rho_{fit,0} + \rho_{fit,1} + \rho_{fit,2}}{3}$$

Where  $\rho_{fit,1}$  denotes the Pearson's correlation coefficient between the fit and the 1<sup>st</sup> trial. The correlation coefficient between trials was determined as the mean of the correlation coefficient of each pair of trials, determined independently for each cell:

$$\rho_{trials} = \frac{\rho_{0,1} + \rho_{0,2} + \rho_{1,2}}{3}$$

Where  $\rho_{0,1}$  denotes the Pearson's correlation coefficient between the first and second trial of all images. This measure defines an upper bound for the variance predictable by the fit.

#### *Moving natural scenes analysis and modeling*

Baseline subtraction was performed as for the white noise analysis. L2 cells with low average response dynamics (quantified as the standard deviation of response throughout a recording) were excluded from further analysis. The responses of each cell to three trials were averaged to obtain a mean response. Trial-to-trial variation ('reliability') was determined as for the static natural scenes for each time point (sampling rate 15 Hz). For all parts of Fig. 5 and S5, we analyzed only the first 6 seconds of the stimulus response (the image moving to the right), and we did not analyze the data of the image moving back.

The luminance model's responses were generated by taking, for each cell, the time series of image luminance values that appeared at the cell's receptive field location. Prior, the images were low-pass filtered with a 2D Gaussian filter with a sigma corresponding to the receptive field size of L2 or Mi1, respectively. In other words, the first model describes a cell with an instantaneous 2D Gaussian filter corresponding to only the center component of the receptive field. The RF model incorporated the 3D filter kernel obtained from the white noise analysis, and thus includes the temporal properties of the cell and the spatial surround in addition to the spatial center. For each cell, the image series was filtered with the 3D kernel to obtain the model responses. The L-NL model consisted of the RF model, and, in addition, a static nonlinearity. To obtain the model's



responses, the output of the RF model was passed through a logistic function. The parameters for the logistic function were determined empirically by fitting the logistic function  $f(x) = b_l + \frac{b_u - b_l}{1 + \exp(-k(x - x_0))}$  to the output of the RF model and the data with the least-squares method (Fig. 5h for L2 and Fig. 5k for Mi1). In order to compare the model responses with the cells' responses, we calculated the Pearson's correlation coefficient between models and data as for the static natural scenes, each time point representing one data point.

## Supplemental references

- Arenz, A., Drews, M.S., Richter, F.G., Ammer, G., Borst, A., 2017. The temporal tuning of the *Drosophila* motion detectors is determined by the dynamics of their input elements. *Curr. Biol.* 27, 929–944.
- Botcherby, E.J., Juškaitis, R., Booth, M.J., Wilson, T., 2008. An optical technique for remote focusing in microscopy. *Opt. Commun.* 281, 880–887.
- Botcherby, E.J., Juškaitis, R., Booth, M.J., Wilson, T., 2007. Aberration-free optical refocusing in high numerical aperture microscopy. *Opt. Lett.* 32, 2007–2009.
- Botcherby, E.J., Smith, C.W., Kohl, M.M., Débarre, D., Booth, M.J., Juškaitis, R., Paulsen, O., Wilson, T., 2012. Aberration-free three-dimensional multiphoton imaging of neuronal activity at kHz rates. *Proc. Natl. Acad. Sci. USA* 109, 2919–2924.
- Brand, A.H., Perrimon, N., 1993. Targeted gene expression as a means of altering cell fates and generating dominant phenotypes. *Development* 415, 401–415.
- Brinkworth, R.S.A., O'Carroll, D.C., 2009. Robust models for optic flow coding in natural scenes inspired by insect biology. *PLoS Comput. Biol.* 5, e1000555.
- Chen, T.-W., Wardill, T.J., Sun, Y., Pulver, S.R., Renninger, S.L., Baohuan, A., Schreiter, E.R., Kerr, R.A., Orger, M.B., Jayaraman, V., Looger, L.L., Svoboda, K., Kim, D.S., 2013. Ultrasensitive fluorescent proteins for imaging neuronal activity. *Nature* 499, 295–300.
- Euler, T., Hausselt, S.E., Margolis, D.J., Breuninger, T., Castell, X., Detwiler, P.B., Denk, W., 2009. Eyecup scope - optical recordings of light stimulus-evoked fluorescence signals in the retina. *Eur. J. Physiol.* 457, 1393–1414.
- Maisak, M.S., Haag, J., Ammer, G., Serbe, E., Meier, M., Leonhardt, A., Schilling, T., Bahl, A., Rubin, G.M., Nern, A., Dickson, B.J., Reiff, D.F., Hopp, E., Borst, A., 2013. A directional tuning map of *Drosophila* elementary motion detectors. *Nature* 500, 212–216.
- Pologruto, T.A., Sabatini, B.L., Svoboda, K., 2003. ScanImage: Flexible software for operating laser scanning microscopes. *Biomed. Eng. Online* 9, 13.
- van Hateren, J.H., van der Schaaf, A., 1998. Independent component filters of natural images compared with simple cells in primary visual cortex. *Proc. Biol. Sci.* 265, 359–366.
- Yang, W., Yuste, R., 2017. In vivo imaging of neural activity. *Nat. Methods* 14, 349–359.